

# A decade of solar Type III radio bursts observed by the Nancay Radioheliograph 1998–2008

P. Saint-Hilaire<sup>1</sup>, N. Vilmer<sup>2</sup>, and A. Kerdraon<sup>2</sup>

*Space Sciences Laboratory, University of California, Berkeley, CA 94720, USA*

*LESIA, Observatoire de Paris, CNRS, UPMC, Université Paris-Diderot 5 place Jules Janssen, 92195 Meudon, France*

shilaire@ssl.berkeley.edu

## ABSTRACT

We present a statistical survey of almost 10 000 radio Type III bursts observed by the Nancay Radioheliograph from 1998 to 2008, covering nearly a full solar cycle. In particular, sources sizes, positions, and fluxes were examined. We find an east-west asymmetry in source positions which could be attributed to a  $6\pm 1^\circ$  eastward tilt of the magnetic field, that source FWHM sizes  $s$  roughly follow a solar-cycle averaged distribution  $\frac{dN}{ds} \approx 14 \nu^{-3.3} s^{-4}$  arcmin<sup>-1</sup> day<sup>-1</sup>, and that source fluxes closely follow a solar-cycle averaged  $\frac{dN}{dS_\nu} \approx 0.34 \nu^{-2.9} S_\nu^{-1.7}$  sfu<sup>-1</sup> day<sup>-1</sup> distribution (when  $\nu$  is in GHz,  $s$  in arcmin, and  $S_\nu$  in sfu). Fitting a barometric density profile yields a temperature of 0.6 MK, while a solar wind-like ( $\propto h^{-2}$ ) density profile yields a density of  $1.2 \times 10^6$  cm<sup>-3</sup> at an altitude of 1  $R_S$ , assuming harmonic emission. Finally, we found that the solar-cycle averaged radiated Type III energy could be similar in magnitude to that radiated by nanoflares via non-thermal bremsstrahlung processes, and we hint at the possibility that escaping electron beams might carry as much energy away from the corona as is introduced into it by accelerated nanoflare electrons.

*Subject headings:* Sun: corona – Sun: radio emission – Sun: particle emission

## 1. Introduction

Particle acceleration events in the quasi-collisionless plasma of the solar corona create supra-thermal electron beams that propagate along magnetic field lines, either away from the Sun into interplanetary space (on so-called “open” field lines), or downwards into the chromosphere (towards the footpoints of magnetic loops). Higher-energy electrons race ahead of the lower energy ones, creating a bump-in-tail instability in the particle distribution. Landau resonance with the unstable electron beams creates Langmuir waves, which are believed to undergo non-linear wave-wave interaction and produce electromagnetic emissions at the local plasma frequency or its harmonic. As the electron beam propagates to higher or lower altitudes (at speeds of  $\approx c/3$  in the low corona, to  $\approx c/10$  at 1 AU, Poquérousse et al. 1996), and hence to lower

or higher densities and plasma frequencies, there is a drift in the frequency of emitted radiation. This coherent plasma emission is generally called a Type III radio burst. Type IIIs have been observed from frequencies as high as  $\approx 1$  GHz at the bottom of the corona to 30 kHz at  $\approx 1$  AU, and even lower further out. Taking only bursts drifting from high to low frequencies, Alvarez & Haddock (1973) have fitted bursts in the 74 to 550 MHz range by the relation  $\frac{d\nu}{dt} \approx -0.01 \nu^{1.84}$  MHz s<sup>-1</sup>.

Nita et al. (2002) have investigated the peak flux distributions of 40 years of spatially-integrated solar radio burst data, from 0.1 GHz to 37 GHz. They have found that the peak flux density distribution of events,  $dN/dS_\nu$ , followed a power-law with a negative index  $\approx 1.8$ , similar to that found in many X-ray studies (for recent work on the topic, see e.g. Hannah et al. 2008).

In this work, we have gathered the solar Type

III peak flux densities, source sizes and positions at different frequencies, observed by the Nançay Radioheliograph (NRH) over the period 1998-Jan-01 to 2008-Apr-01, i.e. covering nearly a full solar cycle.

In Section 2, we describe the data selection process and some of its limitations. We describe the observations in Section 3 and discuss them in Section 4. Finally, in Section 5, we summarize our results and present some conclusions to this study.

## 2. Data selection and caveats

We selected our events from the list of solar radio bursts published by the *National Oceanographic and Atmospheric Administration's National Geophysical Data Center*<sup>1</sup> (NOAA/NGDC), from 1998 January 1 to 2008 April 1, covering almost a full solar cycle. We removed all bursts that were outside the observing times and spectral range ( $\sim 150$ – $450$  MHz) of the *Nançay Radioheliograph* (NRH, Kerdraon & Delouis 1997). We have not gone further than April 2008 because NRH started observing the Sun with a different set of frequencies, and we wanted a consistent set of frequencies for our statistical study. The NOAA list contains information on individual radio bursts, such as reporting station, start and end times and frequencies, as well as spectral type and intensity. This list is compiled from reports, often generated manually, by observers from various ground stations around Earth (Culgoora, Ismiran, Learmonth, Ondrejov, Palehua, Sagamore Hill, San Vito, Bleien, etc.), using spectrometers covering varying bands, from as low as  $\sim 30$  MHz to as high as a few GHz. Hence, certain characteristics such as start and end frequencies, as well as burst intensity, are somewhat subject to both individual spectrometer sensitivity and individual observer's perception. In cases where the same event was reported more than once (by different observatories), only the first such report was kept, and any extraneous ignored. We kept only Type III radio burst reports within the times ( $\approx 8:30$  to  $15:30$  UT, varying during the year) and the spectral band ( $150$ – $432$  MHz) where the NRH was observing the Sun. Groups of decimetric Type IIIs do not last much longer than a few minutes

(individual ones last about one second). Different groups of Type IIIs, even hours apart, are however sometimes bundled together in a single report. Moreover, certain reported time interval are clearly erroneous, probably due to data entry error. We have therefore ignored all Type III reports longer than 10 minutes, (which constituted  $\sim 14\%$  of Type III reports), and were left with 8931 Type III burst reports from 1998 to 2008.

The NRH actually produces images at up to  $1/8$  s temporal resolution, but these are stored on magnetic tapes, and each individual day of data must be retrieved manually. The 10-second data is stored in a file system, and it is therefore much easier and faster to process. This is the reason why it is used in this study. This coarse temporal resolution leads to weak and/or short-duration (such as second-long Type IIIs) bursts being drowned in the solar background. Hence, we have decided to retain only well-determined Type III bursts for this study: those which had peak brightness temperature of 10 MK or above, well above any quiet Sun value. This is the case for 91.4% of cases at 164 MHz, down to 26.2% of cases at 432 MHz. The difference is easily explained by the fact that Type III bursts tend to have lower brightness temperatures at 432 than at 164 MHz (see also §3.3). A priori, the NGDC-reported burst spectral band is not necessarily a good indicator of the actual bandwidth of the Type III burst. (NRH, possessing  $\approx 44$  dishes, is much more sensitive than the single-dish spectrometers that typically report to NGDC). On the other hand, we have empirically observed that taking only bursts either at frequencies for which the peak brightness temperature in the map is above  $\approx 10$  MK, or within the NOAA-reported spectral range, lead to very similar datasets.

The 10-second data used in this study also leads to cases where several individual bursts are being bundled together into a single event. Hence, in this work, a “Type III event” is often “a group of Type IIIs within the same 10-second interval”.

Frequencies 150.9, 164, 236.6, 327, 410.5, and 432 MHz (with a 3-dB bandwidth of 0.7 MHz) were used by NRH during our period of interest. Figure 1 clearly shows a decrease in radio activity as the solar cycle approaches minimum, and the dip in events from 2003 November 5 to 2004 January 25 is due to NRH being off-line while

<sup>1</sup>[http://ftp.ngdc.noaa.gov/STP/SOLAR\\_DATA/SOLAR\\_RADIO/SPECTRAL/](http://ftp.ngdc.noaa.gov/STP/SOLAR_DATA/SOLAR_RADIO/SPECTRAL/)

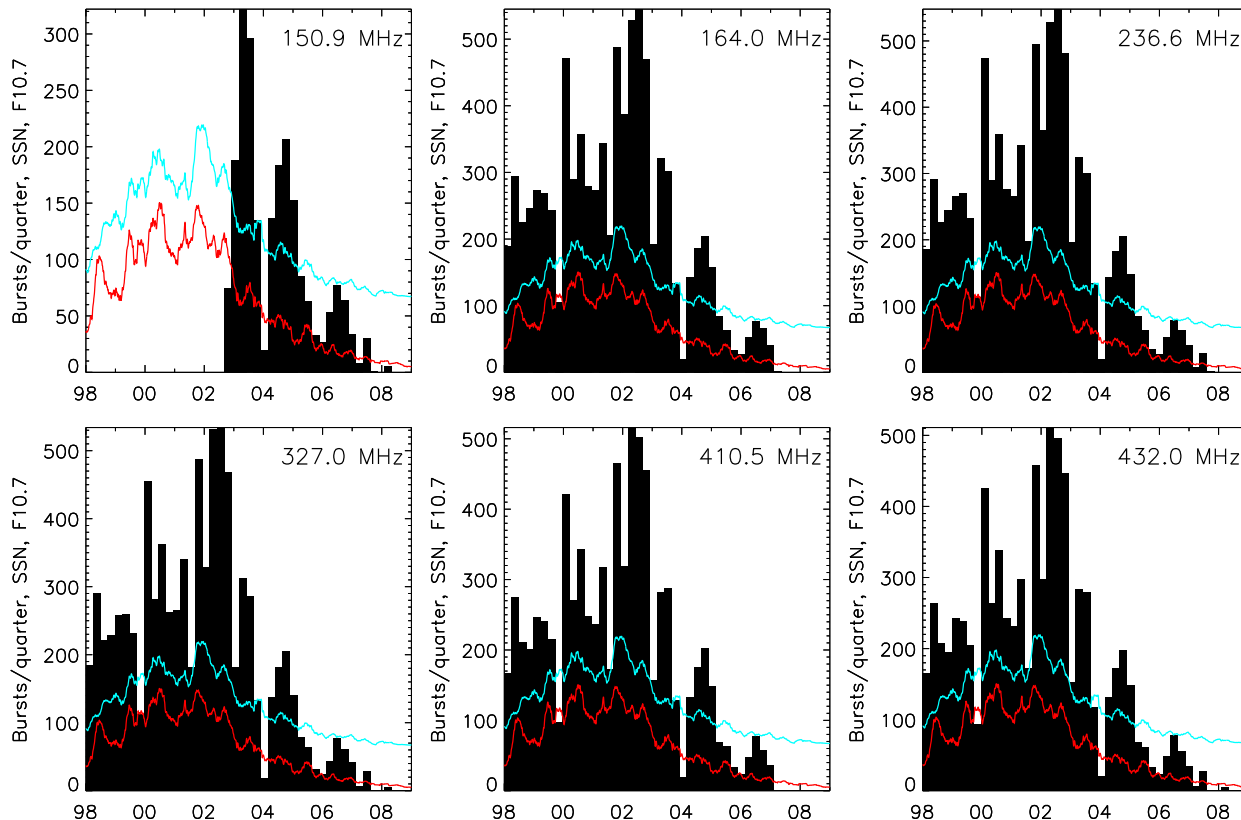


Fig. 1.— *Black*: Time series of the quarterly number of NOAA-reported solar radio bursts, at times and frequencies when and where NRH was observing. *Red*: Sun Spot Number. *Blue*: F10.7 index (in sfu). Three-month time bins or smoothing window were used for all displayed data. NRH was not observing at 150.9 MHz before mid-2002, and was not operating from November 2003 to January 2004 (see text in §2 for more details).

anti-alias antennas were being added to the array. During our decade of interest, the 150.9 MHz frequency has gradually replaced the nearby 164 MHz, no longer reserved under French law. Hence the observations at 150.9 MHz have started later, with an overlap of a few years with the (now no longer used) 164 MHz. **It can be noted that the occurrence rates match qualitatively that of Lobzin et al. (2011), including an almost  $\sim$ two-year periodicity, unexplained so far.** Using NRH 10-second images, and a fixed  $30''$  pixel resolution at available frequencies (this standard coarse resolution, still well below the instrumental resolution at 432 MHz, was chosen for ease of data handling), the following were determined (among other things): time of peak flux density,

location and brightness temperature of brightest pixel in the source, and 2D gaussian fitting parameters to sources present in the image. From the latter, source fluxes can be deduced by computing the gaussian volume. It is important to note that each frequency was treated mostly independently from each other, see §2.1 and 2.2 for a discussion.

Paragraphs 2.1 to 2.6 detail some caveats in our selection and data analysis process.

## 2.1. Time interval of reports:

Firstly, as stated earlier, there can be several Type IIIs temporarily close to one another, within the 10-second accumulation of the data at hand, leading to confusion and averaging of their charac-

teristics. Secondly, our methods looks only for the strongest burst within the NOAA report’s time interval (there can be several inside the time range reported), and does so for each frequency independently. This has for consequence that we are missing any other bursts within the reported time interval, and that the burst characteristics derived at different frequencies might not relate to the exact same Type III burst. About  $\sim 50\%$  of radio bursts from the same report have hence a time difference greater than 10 s between 164 and 432 MHz). This has an obvious effect on the absolute occurrence rates of Type III bursts (they are probably higher than reported here), but we estimate the influence on the power-law shape of their distributions (see §3) to be minimal.

## 2.2. Alias ambiguity:

For bursts occurring before the installation of anti-alias antennas at NRH (between 2003 November 5 and 2004 January 25), there can be an ambiguity in source positions at frequencies above 164 MHz. This is because an alias is sometime present in the reconstructed NRH image, and sometimes has the brightest pixel in the map (particularly when the real source happens to be beyond the solar limb, but the alias lies on top of the solar disk). The distance between the real source and an alias decreases with increasing observing frequency, and any alias is beyond the imaged field of view (and hence no alias ambiguity exists) at frequencies  $\lesssim 164$  MHz. It is usually easy to distinguish between a solar source lasting at least a few minutes and its alias: the alias moves quickly (with time) in a straight line across the solar map. But this method is of little use in our study, as we examine events that seldom last longer than a single 10-second frame. We will instead use the fact that the true source is likely to be spatially near the sources at other frequencies, assuming the radio bursts spans the necessary frequency range. For maps taken at progressively higher frequencies than 164 MHz, we determine whether there is possibility of an alias in the map in the following manner: after locating the source with the brightest pixel, we determine whether there is another source in the map at an appropriate alias position, and with similar peak intensity (within 20%, which corresponds to a 2 MK difference for the minimal 10 MK burst). The “correct” source is

deemed to be the one whose position is closest to the position of the “correct” source in the map of the next lower frequency. This simple method is not perfect: in some cases, emission at lower frequencies is simply not there, because the conditions for plasma emission and/or propagation to Earth are not adequate, and hence, at higher frequencies, the method may home in on other sources.

Before the installation of anti-alias antenna, there was a *potential* alias confusion (two sources of similar intensities, at correct alias positions, as described above) in our data 58% of the time at 432 MHz, progressively lower at lower frequencies, down to 0% at 164 MHz and below.

In summary, source locations before January 2004, low frequencies (150.9 and 164 MHz) should be always accurate, while higher frequencies may have errors in some of the positions, but we expect the impact on the statistical distributions of burst locations (§3.2) to be minimal (see coronal density fittings in §4 for a confirmation). The study of source sizes (§3.1) and fluxes (§3.3) should be unaffected by this issue, as is all the data taken after January 2004.

## 2.3. Bursts fluxes:

The so-called “Quiet Sun” flux is of the order of 10 sfu at NRH frequencies (and brightness temperatures at Sun center of  $\sim 0.7$  MK at 164 MHz). Hence, a lone, 1-sfu, 1-second long Type III burst with area about 1/100 the solar disc (i.e. smeared out to about the size of the NRH beam at 164 MHz, **about 3.2’ FWHM**) would produce an additional surface brightness equal to that of the quiet Sun in a 10-second image. Successfully fitting a gaussian to such a weak burst becomes difficult, and explains the turnover at low fluxes in the distributions presented in §3.3.

## 2.4. Astrophysical sources:

The Crab Nebula, or one of its alias, is the most obvious astrophysical source which can enter the NRH field of view (around June each year). Its surface brightness is similar to the Sun at NRH frequencies, i.e. much lower than the 10 MK threshold used for our selection. Hence, we expect such sources to have little impact in our study.

## 2.5. Refractive effects:

Earth ionospheric refraction can significantly perturb the apparent position of a source in ground-based observatories, sometimes exceeding several arcmins in the 100–300 MHz range (e.g. Bougeret 1981; Mercier 1986). These effects are mostly random position shifts due to ionospheric gravity waves. They are not correlated with the positions of sources on the Sun, and should not affect our statistics. We have therefore ignored those effects in the present study.

## 3. Data Analysis

We have studied in detail the distribution in spatial sizes (§3.1), in positions (§3.2), in fluxes (§3.3), and the rank-order cross-correlations between several of the observables (§3.4).

### 3.1. Burst spatial size distribution:

Radio sources were fitted with 2D elliptical gaussians. These yield *observed* gaussian sizes  $\sigma_{a,obs}$  and  $\sigma_{b,obs}$  (semi-major and semi-minor  $e$ -folding lengths), and a tilt angle  $\theta_{obs}$  of the semi-major axis with respect to the map x-axis (solar east-west). The FWHM values,  $s_{a,obs}$  and  $s_{b,obs}$ , are obtained by multiplication of  $\sigma_{a,obs}$  and  $\sigma_{b,obs}$  with  $2\sqrt{2\ln 2} \approx 2.355$ . In Figure 2, we plot a histogram of the rms averages  $s_{rms,obs} = \sqrt{s_{a,obs}^2 + s_{b,obs}^2}$ . The roll-over at low source sizes is due to the interferometer beamwidth, which is about 3.2–5.5' FWHM at 164 MHz, proportionally smaller at higher frequencies, and varying with the season and time of day.

Assuming that the observed source, the interferometer beam, and the true (deconvolved) source were all elliptical gaussians (with different tilt angles), we have recovered the true source size (see Appendix A for mathematical details), and plotted the results in Figure 3 and their averages in Table 1. Note that some of the largest events (in size) are probably multiple sources, but it was not the purpose of this statistical work to discriminate between such.

As the spectral indices of the distributions for the bursts selected in Section 2 were very close (from 4.4 to 4.9) at all frequencies, we decided to plot the normalization constants  $A_\nu$  as a function of frequency. But to remove any normaliza-

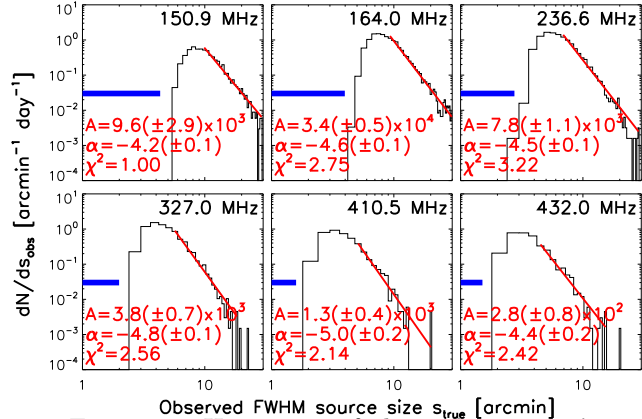


Fig. 2.— Histogram of the radio sources' rms FWHM  $s = s_{rms,obs}$ , at different frequencies. The red curves are fittings  $\frac{dN}{ds} = A s^\alpha$  to the histograms, from the bin to the immediate right of the peak in the histogram and above. The blue bar delimits the *minimum* NRH point spread function (which can vary by almost a factor 2, depending on the season and time of day).

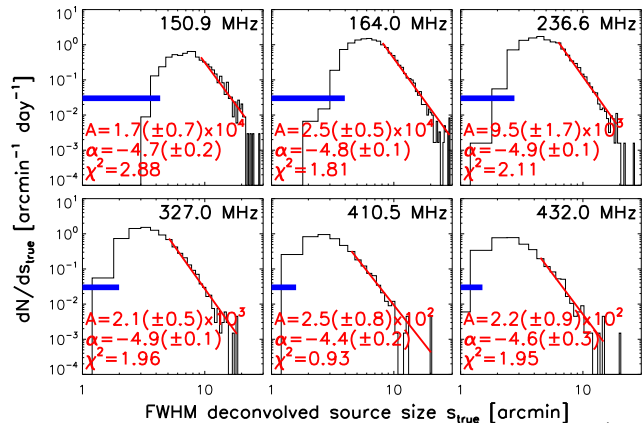


Fig. 3.— As in Figure 2, but displaying *true* (deconvolved) FWHM rms source sizes. The red line and labels are power-law fittings to the data. The blue bar delimits the *minimum* NRH point spread function (which can vary by almost a factor 2, depending on the season and time of day).

tion issue stemming from the fact that not all frequencies were uniformly employed by NRH during the solar cycle (particularly, 150.9 MHz was used only after 2002/10/28), we have used a slightly smaller subset of our data to which we have fitted similar power-laws: we have taken only those events that occurred when NRH was observing at all six frequencies simultaneously, and plotted in

Table 1: Mean and standard deviation of observed and deconvolved (or “true”) source sizes:

Frequency: [MHz]	Observed size [']	Deconvolved size [']
150.9	10.9±4.1	5.3±1.8
164	9.7±3.6	4.5±1.6
236.6	7.0±2.7	3.4±1.3
327	5.2±1.9	2.5±1.0
410.5	4.2±1.6	2.1±0.9
432	3.9±1.6	1.9±0.8

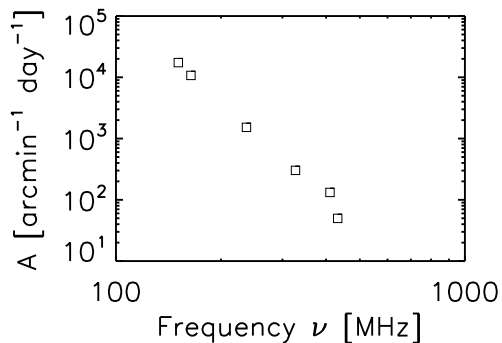


Fig. 4.— Scatter plot of the constants  $A$  obtained from fittings similar to that of Figure 3.

Figure 4 the normalization constants  $A_\nu$  of these new power-law fits. Figure 4 suggests a power-law frequency dependence of the normalization constant  $A \approx B \nu^\beta$ , which has led us to infer that the distribution for true source FWHM size  $s$  could be of the form:

$$\frac{dN}{ds} = B \nu^\beta s^\alpha \quad (1)$$

We have done two-dimensional fittings of our data, using Equation 1 as model. The fitting parameters ( $B, \alpha, \beta$ ) have been found to be moderately dependent on the choice of fitting intervals (and, to a lesser extend, the binning). We therefore prefer to give a range of values for which  $\chi^2$  near unity was obtained: ( $B, \alpha, \beta$ ) from (2.0,-3.0,-2.8) to (20.0,-5.0,-3.8), for an average of  $\approx(7,-4,-3.3)$  over the 2002–2008 period. The result is in  $\text{arcmin}^{-1} \text{day}^{-1}$  if  $\nu$  is in GHz and  $s$  in arcmin. To account for the factor  $\approx 2$  ratio between the 1998–2008 and the 2002–2008 average burst rates (Figure 1), the normalization constant should be changed from 7 to 14 to get a more proper solar-

cycle average.

When the Sun is low on the horizon during certain period of the year, the beam shape can be extremely asymmetric. To insure that these extreme cases have not influenced our results, we have therefore run the same study, removing all events occurring in November, December, and January, as well as all events within two hours of sunset or sunrise during February and October. The differences with the above results were negligible.

A more thorough study of source shape and structure, which would address e.g. cases where more than a single source is present (e.g. Pick et al. 1998, and references therein), is beyond the scope of this paper.

### 3.2. Radioburst location:

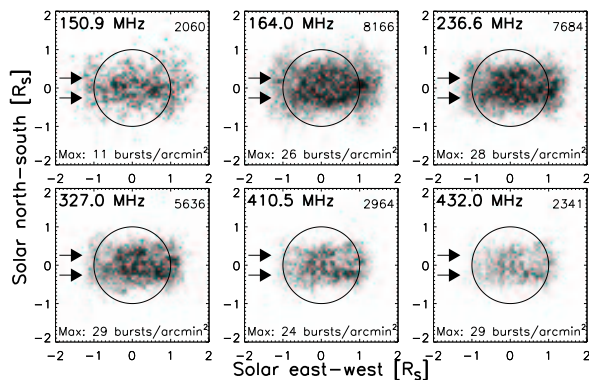


Fig. 5.— Occurrence density distributions for the radio bursts selected in Section 2, on a  $1'$  pixel grid. The number in upper right corner is the total number of events with reliable positions. The intensity scale is linear from white to black, with black representing the maximum pixel value as specified in each plot. The arrows indicate the  $\pm 15$  degrees heliographic latitudes.

Figure 5 shows the distribution of radio bursts for our selected bursts, using the positions that are likeliest to be correct (as discussed in Section 2), while Figures 6, 7, and 8 show the same for three different characteristic years in the solar cycle.

The most striking feature is, at high frequencies, the concentration of radio bursts in two distinct bands (around latitudes  $\pm 15$  to  $\pm 30$  degrees for 432 MHz) during early solar maximum years (Figure 6), and at lower latitudes as the solar cycle advances. This is in remarkable agree-

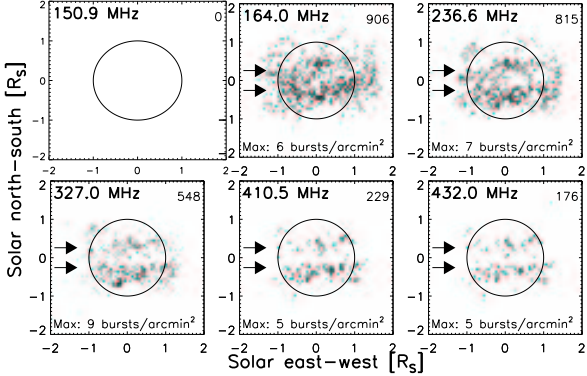


Fig. 6.— As Fig. 5, taking only events that occurred in 1998. No observations at 150.9 MHz were made that year.

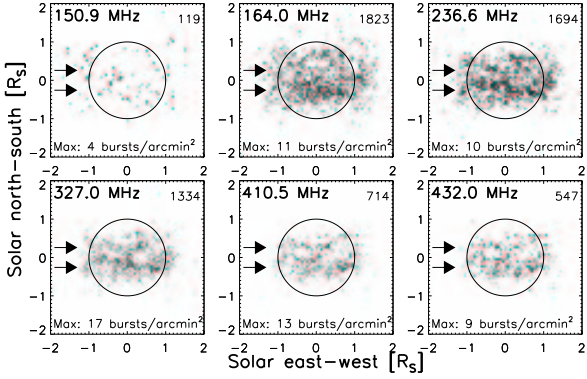


Fig. 7.— As Fig. 5, taking only events that occurred in 2002.

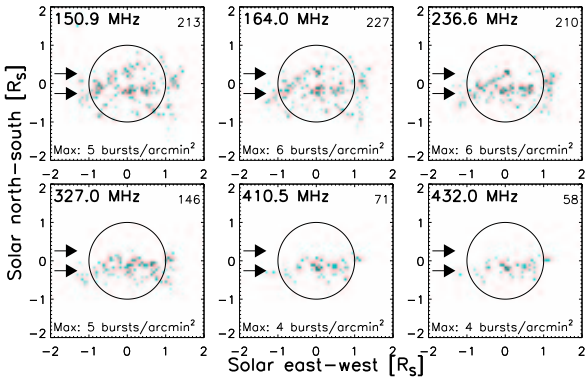


Fig. 8.— As Fig. 5, taking only events that occurred in 2006.

ment with observed active region and microflare positions and their solar-cycle dependence (e.g. Christe et al. 2008a). Later in the solar cycle, bursts are located mostly south of the solar equa-

tor, just as active regions were (Higgins et al., 2012, *in preparation*).

The second most striking feature is the systematic shift of about  $2' = 120''$  westward of the mean position of all radio bursts (Figure 9). While a systematic shift of instrumental origin of up to  $0.3'$  westward for all frequencies was expected (from comparison between VLA and NRH positions of a radio spike – *priv. comm. P. Grigis.*), clearly it cannot account for all of the observed shift.

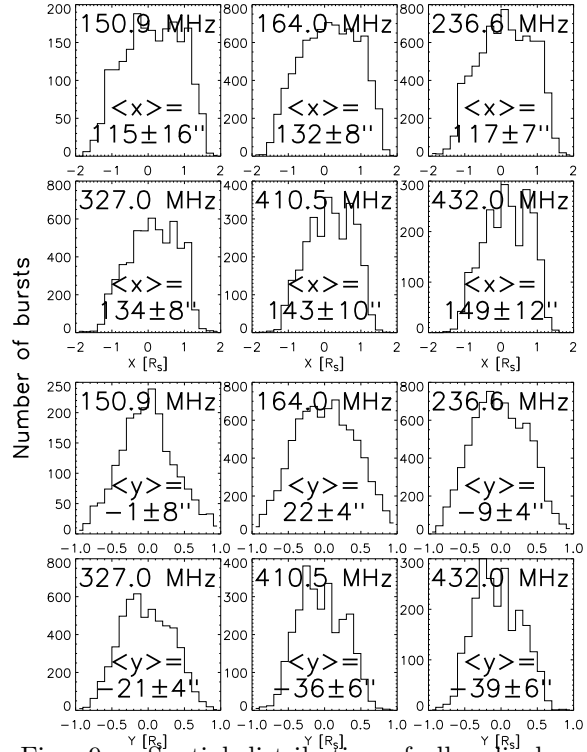


Fig. 9.— Spatial distribution of all radio burst positions between 1998 and 2008: histograms for all six frequencies (*top six*: east-west coordinate, *bottom six*: north-south coordinate) with means and their errors. A westward shift between 115 and 149'' can be observed at different frequencies.

### 3.3. Source peak brightness temperatures and fluxes

In this section, we investigate the distribution of “peak” (in terms of 10-second averages) brightness temperature  $T_B$  (in K) and source fluxes  $S_\nu$  (in sfu, where  $1 \text{ sfu} = 10^{-22} \text{ W m}^{-2} \text{ Hz}^{-1}$ ). Figures 10 and 11 show that the peak brightness temperatures and fluxes of our radio bursts, follow a

$\frac{dN}{dS_\nu} \propto S_\nu^{-1.7}$  law, very close to what Nita et al. (2002) found. Equivalently, the number of bursts above  $T_B$  or  $S_\nu$  follow a power-law with negative index one higher (see Figure 12 for  $S_\nu$ ). The roll-over at low fluxes is most likely due to our selection criteria (see discussion in §2).

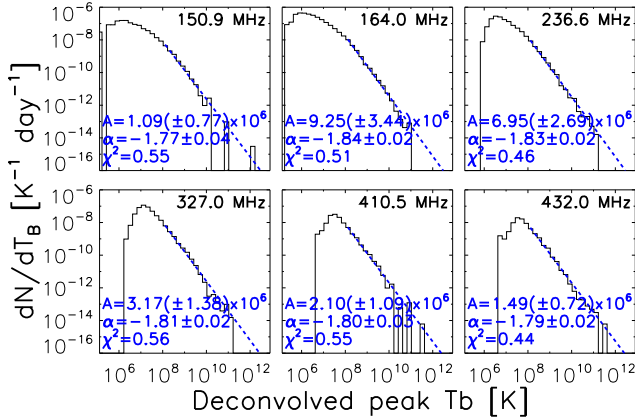


Fig. 10.— Histogram of deconvolved (i.e. assuming both observed and true sources are gaussian-shaped) peak brightness temperature of all Type III bursts. The dashed blue line is a power-law  $\frac{dN}{dT_B} = AT_B^\alpha$  fit to the data, using the C-statistic (Cash 1979), technically better suited than Poisson statistics for datasets with small number of counts per bin (as is our case for the high-value bins, but in this case leading to negligible differences). The associated best-fit parameters are in the lower left corner.

Note that unresolved sources always have lower brightness temperature than their “real brightness” temperature, and that a source’s “real” brightness temperature is always smaller or equal to its true temperature (opacity). For these reasons, the flux  $S_\nu$  is probably a less misleading quantity to use than  $T_B$ , and we will concentrate on  $S_\nu$  in the remainder of this section.

As the spectral indices in Figure 11 at different frequencies were very close, we decided to plot the normalization constants  $A_\nu$  as a function of frequency (Figure 13). As with the source sizes in §3.1, we have taken a subset of our data, using only events occurring when NRH was observing with all six frequencies. Power-law fittings to these new distributions yield more meaningful normalization constants  $A_\nu$ , plotted in Figure 13. Again, notice that the coefficients  $A_\nu$  appear to have a power-law dependence with frequency:  $A_\nu \approx B\nu^\beta$ . We

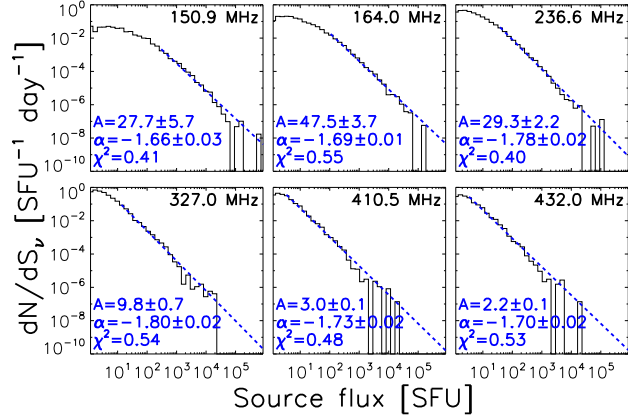


Fig. 11.— Histogram of gaussian source fluxes (averaged over 10 seconds), with power-law fittings  $\frac{dN}{dS_\nu} = AS_\nu^\alpha$  using the C-statistic (Cash 1979).

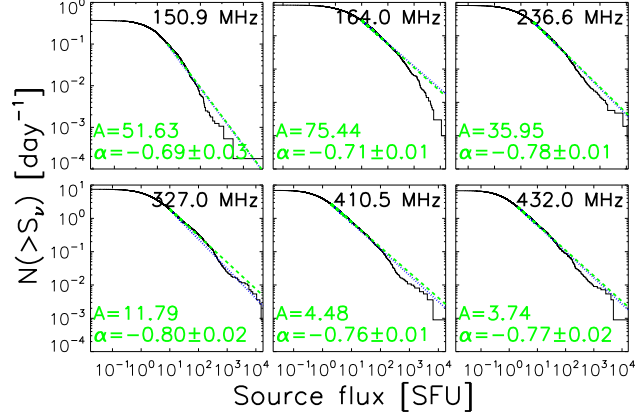


Fig. 12.— Cumulated data  $N(> S_\nu)$ . The blue dotted line is the integral of the fitting found in Figure 11, while the green dashed line and coefficients are derived from the Maximum-likelihood method of Crawford et al. (1970). They match almost exactly.

have therefore attempted to fit all our data with the following model:

$$\frac{dN}{dS_\nu} = B\nu^\beta S_\nu^\alpha \quad (2)$$

The best-fitting parameters for the 2002–2008 period were found to be (with  $\nu$  expressed in GHz, and  $S_\nu$  in sfu):  $B=0.17\pm0.01 \text{ sfu}^{-1} \text{ day}^{-1}$ ,  $\alpha=-1.7\pm0.05$ ,  $\beta=-2.9\pm0.1$ . These fitting parameters have proven to be very stable (and all with near unity  $\chi^2$ ) even if changing fitting intervals, and hence much more robust than those found in Section 3.1 for size distributions. To account for the



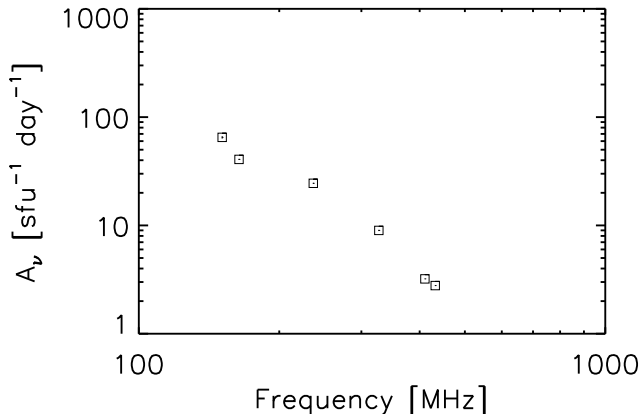


Fig. 13.— Plot of the normalization coefficients  $A$  for fittings similar to Figure 12, but taken only over times when all six frequencies were observing, as a function of frequency.

factor  $\approx 2$  ratio between the 1998–2008 and the 2002–2008 average burst rates (Figure 1), the normalization constant should be changed from 0.17 to 0.34 to get a proper solar-cycle average.

It is well known that more Type III bursts are seen at low frequencies than at high frequencies, and the above relationship reflects this. **In fact, Dulk et al. (2001) found the spectrum of a Type III burst in the 3–50 MHz range to have a negative spectral index close to 3, in good agreement with our results.**

### 3.4. Rank-order cross-correlations:

We cross-correlated most of the observables mined from our study. The results and method of correlation are described in Appendix E. The only noteworthy relationship that we have observed is the anti-correlation between the “radial elongation” (the ratio of the deconvolved source size in the radial direction over the deconvolved rms source size) of sources and the radial offset from Sun center (Figure 14). This anti-correlation means that sources tend to be circular near disc center, and elliptical near the limb, with minor axis along the radial direction. We will discuss the implications of this mild correlation in the next Section.

There is a noteworthy absence of strong correlation between the source flux  $S_\nu$  and the source size  $s_{true}$ , which will also be discussed in Section 4.

Due to the longer path in the corona that emis-

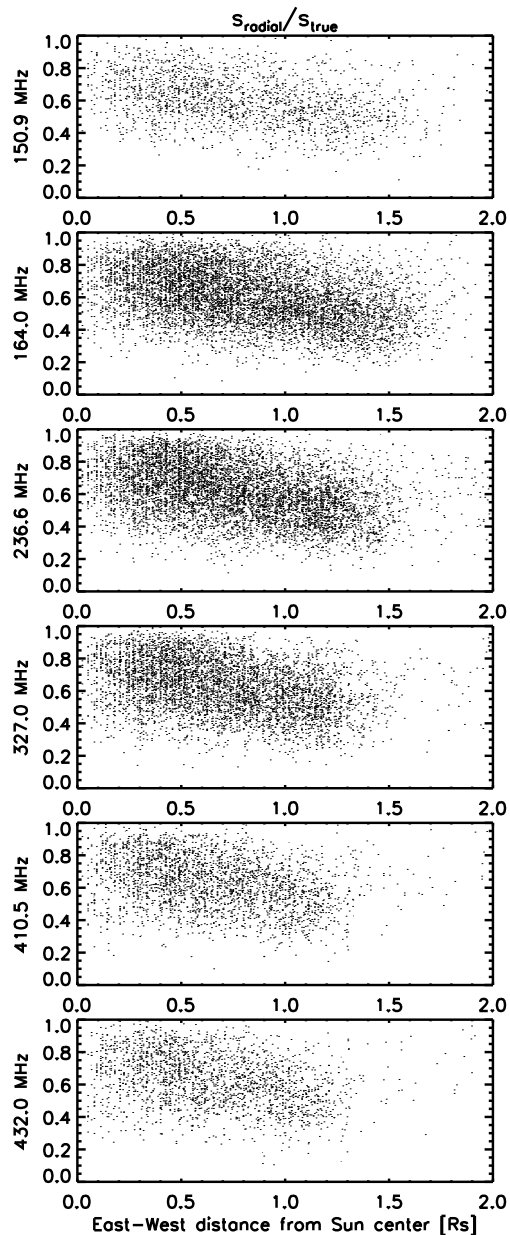


Fig. 14.— Scatter plot of radial distance vs. “radial elongation” (ratio of deconvolved source size in the radial direction over deconvolved rms source size) of sources. The mild anti-correlation indicates that, the further away from Sun center, the more elongated in the direction perpendicular to the radial sources tend to be.

sions from sources near the limb have than those near disk center, it is expected that turbulent scattering would make them appear slightly larger on average than their on-disk brethren (Bastian

1994). There appears to be indeed a slight correlation ( $\approx 0.2$ ) between deconvolved source size  $s_{true}$  and angular distance  $r$  from Sun center in our data (particularly at the lower frequencies).

#### 4. Discussion

**Source sizes:** The variation of source sizes with frequency relies on a convolution of different effects: the magnetic field structure opening as a function of height in the corona, the fact that we may have several different Type IIIs at slightly different locations in the same 10-second time interval, the distribution of intrinsic spatial width of the electron beam (Bastian 1994, considered point sources in his work), and, of course, a host of (mostly refractive in origin) propagation effects (see e.g. Poquérusse & McIntosh 1995; Dulk 2000, for recent overviews). For example, true source sizes could be 3.5 (harmonic) to 1.7 (fundamental) smaller than observed, according to Melrose (1989).

Average values of Type III burst sizes have been measured at frequencies below 169 MHz in the 1970s-1980s (Bougeret et al. 1970; Stewart 1974; Dulk et al. 1979; Dulk & Suzuki 1980). They are found to increase with decreasing frequencies and, on the average, to be of the order of 5' at 169 MHz (values between 2' and 7', see also Zlobec et al. 1992; Mercier et al. 2006), which compares well with the  $4.5 \pm 1.6'$  value in Table 1. The first spatially resolved observations of Type III bursts at high time resolution with the Nançay Radioheliograph showed that Type III bursts can be resolved into narrow components (Raoult & Pick 1980) (elementary size of the order of 2') with a typical size which increases with time during the burst, potentially reaching 5' to 7' at then end of the burst. What we have measured in the present paper where we do not use high time resolution data will reflect more the total size of the whole Type III burst group rather than the size of individual components. Systematic studies of burst sizes have been performed only at 164 MHz (Raoult & Pick 1980; Pick & Ji 1987). The distribution of east-west sizes showed that Type III bursts may be resolved in a few cases in components with real sizes around 2', but that the distribution of sizes can reach 9'. The present study provides the first information on the sizes of Type III bursts at fre-

quencies above 169 MHz. It shows that Type III bursts are smaller at high frequencies than at low frequencies and that the size decreases as  $\nu^{-3.3}$ .

Theory (e.g. Bastian 1994, and references therein) predicts that scattering of the emission in the solar atmosphere would lead to a  $\nu^{-2}$  dependence of the source size. This has been confirmed by observations of cosmic sources through the solar corona (Erickson 1964; Coles & Harmon 1989). However, previous observations have showed a quasi-linear dependency of Type III source sizes (from  $\approx 0.1$  to  $\approx 1500$  MHz) with wavelength (Steinberg et al. 1985; Dulk 2000). Our observations support neither.

Although he himself states his analysis becomes invalid for radio wavelengths longer than a few dm, Bastian (1994) predicts a sizeable increase of source sizes near the limb. The fact that we seem to observe only little of it might be an indication that there is a cutoff in the level of turbulence. I.e. that below a certain altitude, turbulence would no longer be proportional to the ambient density as it is for distances greater than  $1.7 R_S$ .

**Weak correlation between source sizes and fluxes:** This is consistent with the interpretation that emission comes from a spatially small region and that propagation effects (see e.g. Poquérusse & McIntosh 1995, for a short overview) are responsible for the lack of good correlation. Notice, however, that the correlation coefficient gradually improves at higher frequencies (from 0.08 at 164 MHz to 0.35 at 432 MHz), suggesting that these (refractive) propagation effects become less important at higher frequencies.

**Source anisotropy near the limb:** The slight anisotropy observed as sources get nearer to the limb can be interpreted as being due to the fact that they are being observed more edge-on than when at Sun center, and that the emitting layer is thinner than the horizontal source size.

**Source location:** Type III emission at the local plasma frequency (fundamental) is expected to be radiated primarily in a dipolar pattern, perpendicular to the local magnetic field. For radiation at the harmonic, a quadrupolar pattern is expected. However, the propagation of radio waves

is controlled both by large and small scale structures which can modify the primary directivity of the radio emission through respectively refraction (including ducting, Duncan 1979) and scattering processes. Particularly, emission at the fundamental tends to become aligned with the local density gradient. See e.g. Zheleznyakov & Zaitsev (1970); Melrose (1986); Cairns (1987a,b); Robinson et al. (1994) for theoretical work, Poquérusse & McIntosh (1995) for a recent short overview, and Thejappa et al. (2012) for recent observational work.

The first investigation of the directivity of Type III bursts was achieved by Caroubalos & Steinberg (1974); Caroubalos et al. (1974) using stereoscopic measurements at 169 MHz obtained simultaneously with the STEREO-1 experiment and with the NRH. Some directivity was found for the Type III bursts (especially for the fundamental emission). The directivity was however found to be less than for Type I bursts. Stereoscopic measurements of the directivity have then been performed using ground-based measurements at 150 MHz and measurements on ULYSSES in the 1.25–940 kHz range (Poquérusse et al. 1996; Hoang et al. 1997). They found that the average pattern of the Type III bursts at low frequencies is shifted  $40^\circ$  eastward of the radial direction. The shift and width is found to decrease with low frequencies. Bonnin et al. (2008) further investigated the directivity of Type III bursts in the interplanetary medium using calibrated Wind-Ulysses observations in the same frequency range. They confirmed an eastward shift of  $23^\circ$  at 940–740 kHz and  $55^\circ$  at 55–104 kHz, i.e. increasing with wavelength. In all these papers, the shift is attributed to a transverse density gradient created by the fast wind (propagating along spiraled open field lines) overtaking the (mostly radial) slow wind. At meter wavelengths, an east-west asymmetry for noise storms was reported by Fokker (1960, 1963); Suzuki (1961); Le Squeren (1963), (see Elgarøy 1977, pp.111–115, and references within for a review). The asymmetry is about 0.1 Rs towards the west. One of the possible explanations which was proposed is that there is a tilt towards the east in the magnetic structures.

In the present study performed at decimetric/metric wavelengths, we do not observe a  $\propto \lambda$  behaviour of the westward shift in our dataset, but this could be due to the fact that NRH observes

bursts at much higher frequencies and much closer to the Sun. On the other hand, combining the observed  $\approx 2'$  westward shift with a simple geometric model (details in Appendices C), an average tilt angle between the direction of emission and the radial to Sun center can be derived, and has been found to be around 6 degrees. (This result is consistent with a more elaborate model using a Monte-Carlo approach, detailed in Appendix D.) This is in the same order of magnitude as was found from noise storms asymmetries. If one assumes that the optimal direction of emission **statistically** corresponds to the direction of the local magnetic field, one hence concludes that the magnetic field is on average tilted eastward by  $\approx 6^\circ$  with respect to the radial direction, at altitudes of a few tenths of a solar radius, where emission at 150–432 MHz occurs.

**Derivation of coronal density profile:** In the following, we assume that emission is either at the fundamental or the harmonic of the local plasma frequency, though the latter is generally thought to be the dominant emission mechanism in the case of decimetric Type III emission. Using position data after 2004/01/25 (the best position data, obtained after the installation of anti-alias antennas), it is possible to derive statistically the average height difference between emission at different frequencies. See Appendix A of Saint-Hilaire et al. (2010) for comprehensive details of the method. This method assumes that sources at different frequencies tend to be radially distributed at different heights. The effect of the small  $\approx 6^\circ$  tilt angle is neglected. In the first five panels of Figure 15, we have plotted all average  $R$  (plane-of-sky, or POS, distance from Sun center) vs.  $\Delta R$  (POS distance between centroid at two different frequencies) for emission at 150.9 MHz versus the other five frequencies. The fitted slopes are proportional to the average height difference (the nearer to disk center, the smaller the height difference, and the nearer to the limb; the larger the height difference). Note that the line *must* go through the origin, making the fittings much stronger than initially appears. The height differences are plotted in the last panel of Figure 15. We have fitted two simple density profiles to this data:

1. A hydrostatic exponential atmospheric  $n =$

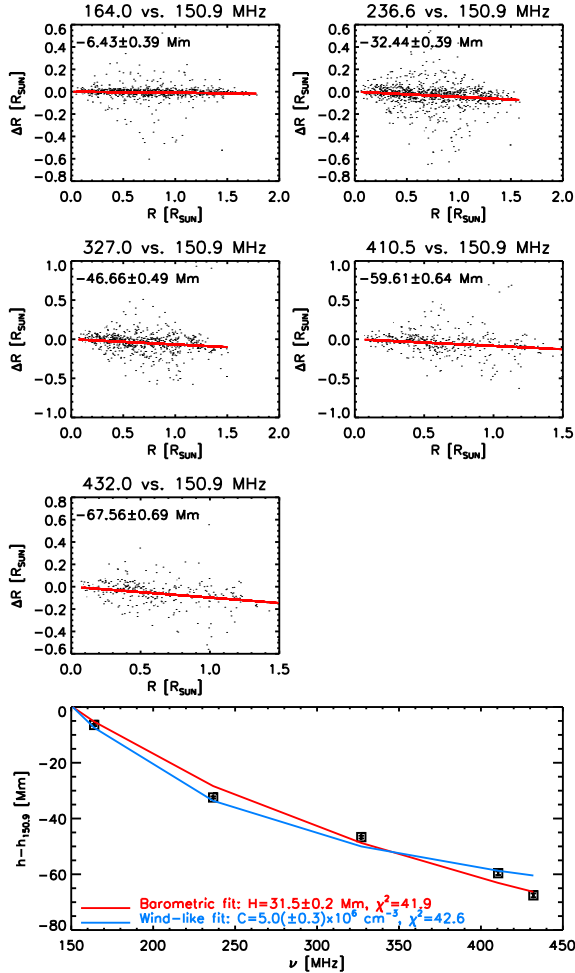


Fig. 15.— Using the methodology presented in detail in Appendix A of Saint-Hilaire et al. (2010), we have statistically derived the relative heights between emission at different frequencies (first five plots). In the bottom plot, we have plotted the height differences, with error bars, and fitted simple density profiles. See text for details.

$n_0 e^{-h/H}$  model (where  $H$  is the scale height, and  $h$  the altitude above the photosphere), which, in order to be used on our data, is transformed into:

$$\Delta h_{ij} = h_i - h_j = -2H \ln \frac{\nu_i}{\nu_j} \quad (3)$$

Where  $i, j$  refer to different frequencies of observations. Note that this model is not influenced by whether the emission is at the fundamental or harmonic of the local plasma frequency. Best fitting yields  $H = 31.5$  Mm

(the red curve in the bottom plot of Figure 15). This scale height corresponds to a  $\approx 0.6$  MK corona, lower than the more usual quiet Sun values of 1–1.5 MK. This could be due to the fact that we are observing Type IIIs near regions of open field lines, and/or the fact that we are near altitudes where solar wind-like conditions start to take over. David et al. (1998) indeed found very low temperatures at similar heights in polar coronal holes.

2. A “solar wind-like” atmosphere  $n(h) = C(h/R_S)^{-2}$  model (Cairns et al. 2009), which, in order to be used on our data, is transformed into:

$$\Delta h_{ij} = h_i - h_j = 8980 m R_S \sqrt{C} \left( \frac{1}{\nu_i} - \frac{1}{\nu_j} \right) \quad (4)$$

Where  $m=1$  or 2 for emission either at fundamental or harmonic. The normalization constant  $C$  can be viewed as the electron density at an altitude of  $1 R_S$ . Best fitting yields  $C = 5 \times 10^6 \text{ cm}^{-3}$  (emission at fundamental) and  $C = 1.2 \times 10^6 \text{ cm}^{-3}$  (emission at harmonic), and the blue curve in the bottom plot of Figure 15. The numbers for harmonic emission are comparatively low, while for fundamental emission, they are comparable to the Baumbach–Allen formula and other published work: e.g. Newkirk (1961); Mann et al. (1999) for theoretical models, and see Fainberg & Stone (1974) and Aschwanden & Acton (2001) for a recent compilation of observational work.

Note that we have also used the pre-2004 data, and have found there was very little difference with the “better” post-2004 data. Both fittings appear equally good (or equally bad), and this methodology cannot decisively choose which of these two models is the most appropriate.

**Source intensities and fluxes:** Maximum observed brightness temperature  $T_B$  in interplanetary Type III bursts are reported to be  $\approx 10^{15}$  K, and up to  $\approx 10^{12}$  K for coronal Type III bursts (Melrose 1989). We observe a few events  $> 10^{11}$  K in our dataset.

We have found a power-law dependence of the occurrence rate of Type III bursts of peak flux  $S_\nu$

with a negative spectral index of 1.7, very similar to Nita et al. (2002), and to what is found in X-rays for flare energies (Crosby et al. 1993; Hannah et al. 2008). Eastwood et al. (2010) have found a 2.1 index for interplanetary Type III solar radio storm in the 0.125-16 MHz range.. A 1.7 negative power-law index is also an oft-seen value in self-organized criticality (SOC) studies: Bak et al. (1988); Lu & Hamilton (1991); Vlahos et al. (1995); Georgoulis & Vlahos (1996); Aschwanden (2012). In their study of Type I noise storms, Mercier & Trottet (1997) had found negative power-law spectral indices of about 3 to 3.5 for their  $\frac{dN}{dS_\nu}$ , and have attributed it to the predicted low-energy part of SOC theory (Vlahos et al. 1995). (Type I noise storm bursts are indeed less energetic but much more frequent than the decimetric Type III bursts studied here.) Similarly, Morioka et al. (2007) found a -3.6 index for interplanetary ( $\approx$ MHz) “micro-type-III” bursts.

Additionally, we find a  $\propto \nu^\beta$  (with  $\beta \approx 2.9$ ) spectral dependence of  $\frac{dN}{dS_\nu}$ , reflecting the fact that Type IIIs are more easily observable, or occur more often, at 164 MHz than at 432 MHz. This exponent could provide constraints to Type III emission models such as in Robinson & Cairns (1998); Melrose (1989).

**Solar-cycle averaged radiative output:** To put things in perspective, we compared the global energy radiated by the Type III bursts and the energy input of flares into the corona. We have plotted in Figure 16 the “**Radio Burst Occurrence Rate**” (RBOR) of our observed Type IIIs and compared it to the energy input from EUV/X-ray events to the corona, derived in other studies (see e.g. Hudson 1991, for a discussion on this topic). The RBOR can be estimated from the power-law fitting parameters by using the  $\frac{dN}{dS_\nu}$  at 164 MHz (Figure 11), by assuming a burst bandwidth of  $\Delta\nu \approx 300$  MHz (Islaker & Benz 1994), taking  $\Delta t=10$  seconds (since all our numbers are 10-second averages), and computing the total energy radiated as observed from  $D=1$  AU. We have further normalized to the photospheric surface area, in order to compare to the “Flare Frequency” often used in coronal heating studies:

$$RBOR = \frac{1}{4\pi R_\odot^2} \frac{1}{4\pi D^2 \Delta\nu \Delta t} \frac{dN}{dS_\nu} \quad (5)$$

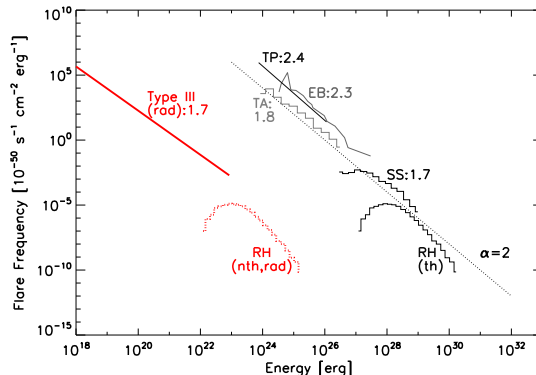


Fig. 16.— *Black/gray*: Approximate flare heating input to the solar corona as derived from various EUV/X-ray nanoflare and microflare studies: *RH*: *RHESSI*, Hannah et al. (2008); *SS*: *Yohkoh SXT*, Shimizu (1995); *TA*: *TRACE*, Aschwanden et al. (2000); *TP*: *TRACE*, Parnell & Jupp (2000); *EB*: *SOHO EIT*, Benz & Krucker (2002) (after Hannah et al. 2008). *Red lines*: Radiated energies. The dotted red line corresponds to the radiated energy in non-thermal HXR that roughly accompanied the *RHESSI*-derived flare input, using an approximated nonthermal bremsstrahlung efficiency of  $10^{-5}$ . The solid red line is the radiated energy derived from this Type III study.

(Note that  $4\pi D^2 \Delta\nu \Delta t dS_\nu = dE$  is the radiated energy for one event). The RBOR is hence the occurrence rate of radiated energy distribution of Type III events, per unit (photospheric) solar area. One notices that the *radiated* energy by decimetric Type IIIs is about five to six orders of magnitude less than the energy input by EUV nanoflares in the corona (we loosely refer to flares observed in EUV only as “nanoflares”, and those observed also in X-rays as “microflares” or “flares”), about the same ratio that exists between the non-thermal hard X-ray (HXR) emission associated with X-ray flares and microflares, though the emission mechanism is believed to be vastly different (coherent plasma emission vs. bremsstrahlung). Ramesh et al. (2010) have estimated that a 40 sfu metric (77 MHz) interplanetary Type III burst was produced by a  $\approx 3 \times 10^{24}$  ergs electron beam. Using the same assumptions on  $\Delta\nu$ ,  $\Delta t$ , and  $D$  as before, this would imply an efficiency of non-thermal radiated energy over beam energy of  $\approx 10^{-5}$  (within an order of magnitude). It is interesting to note

that this ratio is somewhat similar to the one between radiated non-thermal X-rays and the energy in thick-target (Brown 1971) accelerated electrons (see Appendix B). To our present knowledge, there is no obvious reason for the non-thermal bremsstrahlung efficiency (an incoherent process) and the efficiency of Type III plasma emission (a collective process) to be similar, and it may be a coincidence. Clearly, more studies are needed to ascertain radiative efficiencies, but assuming they are indeed similar, this has for consequence that nanoflare and possibly microflare electrons could be similar in number and energies as Type III-producing escaping coronal electron beams! This is in contradiction with recent studies (Christe et al. 2008b; Saint-Hilaire et al. 2009), which have shown that there is probably a factor  $\approx 500$  more flare electrons than escaping electrons. However, note that these studies were centered on one-to-one association of precipitating flare electron beams and escaping interplanetary electron beams (loosely assuming that interplanetary beams and their counterparts in the low corona have similar properties), while the present study is more global (and, for example, it allows for temporal displacement between the two phenomena and different rates of occurrence). One of the implications is that escaping electron beams carry energy away from the corona, partially or wholly negating coronal heating by nanoflares. We dare not speculate any further without a better handle on radiative efficiencies of Type III-producing electron beams. The upcoming NuStar mission (Harrison et al. 2005), and perhaps also the FOXSI rocket flight, should reveal how many electrons are in Type III beams (via their X-ray emission), yielding the efficiency of Type III radio emission.

## 5. Summary, conclusions, and future work

We have studied solar Type III radio bursts observed by NRH during 1998–2008, almost a full solar cycle. From this very rich dataset, we have determined source sizes, locations, fluxes, and their frequency distributions.

The source size distribution  $\frac{dN}{ds}$  can be fitted with a double power-law in  $\nu$  and in  $s$ . The Type III burst sizes are found to decrease as  $\nu^{-3.3}$ , which could reflect a combination of the magnetic field opening as a function of height in the corona,

and the distribution of the spatial widths of electron beams in the corona.

The source flux distribution follows a -1.7 power-law at all frequencies. A two-dimensional power-law fitting yields  $\frac{dN}{dS\nu} \propto \nu^{-2.9} S\nu^{-1.7}$ . These values offer additional constraints to theoretical models of Type III emission.

Type III emission generally come from active regions (just as flares), and we have observed an east–west asymmetry in their location, which could be explained by an eastward tilt of the magnetic field (compared to the local radial to suncenter) at the typical height where our metric/decimetric Type III emission occurred. We have estimated that the tilt angle is about  $\approx 6^\circ$  at altitudes  $\approx 0.3$ – $0.6 R_S$ .

A barometric fit to the data led to a  $\sim 32$  Mm scale height, and temperatures similar to what can be found in coronal holes, while fitting a solar-wind like density profile yielded a density of  $\frac{5 \times 10^6}{m^2} \text{ cm}^{-3}$  (where  $m$  is the harmonic number) at an altitude of  $1 R_S$ .

Furthermore, we speculated that the solar-cycle averaged radiated Type III energy output could be similar to that of radiated non-thermal bremsstrahlung from accelerated nanoflare electrons. We further suggest that escaping electron beams could be a viable mechanism for carrying energy away from the corona, in a quantity similar to the energy introduced into it through nanoflares, though this result depends heavily on as yet unknown radio radiative efficiencies.

It is likely that statistical testing of the different theoretical models of the generation and propagation of Type III bursts (e.g. Dulk et al., 1979; Duncan, 1979; ...; Robinson & Cairns, 1998) could be done. In particular refractive effects on apparent source sizes, locations, and fluxes. Possible other future work includes the usage of sub-second or the full 128 ms resolution data, if it ever becomes easily usable (e.g. stored on a file system instead of on tapes). After the development of a good (and automated) Type III burst detection and discrimination (e.g. Lobzin et al. 2009), this work could be repeated almost verbatim. In the meantime, it is envisaged to do a statistical comparison between the Type III bursts in this work and the X-ray flare parameters found in the RHESSI flare or microflare lists, and get

observational constraints on radiative efficiencies by comparing with in-situ measurements of electron beams associated with the metric/decimetric Type III emissions presented in this work.

### A. Convolution of two elliptical gaussians with different tilt angles.

The convolution of a gaussian elliptical source (semi-major axis  $a_{true}$ , semi-minor axis  $b_{true}$ , and tilt angle  $\theta_{true}$ ) with a gaussian elliptical beam ( $a_{beam}$ ,  $b_{beam}$ ,  $\theta_{beam}$ ) yields an observed source that is also an elliptical gaussian ( $a_{obs}$ ,  $b_{obs}$ ,  $\theta_{obs}$ ). Through Fourier transformation, the following can be derived:

$$\tan(2\theta_{true}) = \frac{(a_{obs}^2 - b_{obs}^2) \sin(2\theta_{obs}) - (a_{beam}^2 - b_{beam}^2) \sin(2\theta_{beam})}{(a_{obs}^2 - b_{obs}^2) \cos(2\theta_{obs}) - (a_{beam}^2 - b_{beam}^2) \cos(2\theta_{beam})} \quad (\text{A1})$$

$$a_{true} = \sqrt{\frac{1}{2}(a_{obs}^2 + b_{obs}^2 - a_{beam}^2 - b_{beam}^2 + \Delta)} \quad (\text{A2})$$

$$b_{true} = \sqrt{\frac{1}{2}(a_{obs}^2 + b_{obs}^2 - a_{beam}^2 - b_{beam}^2 - \Delta)} \quad (\text{A3})$$

with:

$$\Delta = \frac{(a_{obs}^2 - b_{obs}^2) \cos(2\theta_{obs}) - (a_{beam}^2 - b_{beam}^2) \cos(2\theta_{beam})}{\cos(2\theta_{true})} \quad (\text{A4})$$

$$\text{or } \Delta = \frac{(a_{obs}^2 - b_{obs}^2) \sin(2\theta_{obs}) - (a_{beam}^2 - b_{beam}^2) \sin(2\theta_{beam})}{\sin(2\theta_{true})} \quad (\text{A5})$$

(use whichever has non-zero denominator).

Moreover, an important result, which can be derived by combining Eqs (A2) and (A3):

$$s_{obs}^2 = s_{true}^2 + s_{beam}^2 \quad (\text{A6})$$

where  $s_i^2 = a_i^2 + b_i^2$ , with  $i$  being *obs*, *true*, or *beam*. I.e., when dealing with the convolution of elliptical gaussians, the rms size of the observed source is simply the quadratic mean of the rms size of the beam and of the true source, independent of any tilt angle between the true source and the beam.

### B. Non-thermal bremsstrahlung efficiency in the case of the thick-target model:

For an injected electron spectrum with negative spectral index  $\delta$  and low-energy cutoff  $E_c$ , and assuming non-relativistic cross-sections for bremsstrahlung (Bethe-Heitler) and energy losses, the ratio of total emitted X-ray energy over accelerated electron energy can be approximated by the following analytical expression, derived by considering the photon spectrum to be a power-law above a low-energy cutoff  $E_c$ , and a flat spectrum below it:

$$\eta \approx \frac{4}{3\pi} \frac{\alpha}{\Lambda} \frac{1}{z^2} \frac{1}{m_e c^2} \frac{B(\delta/2, 1/2)}{\delta - 1} f^{-\delta+2} \left(1 + \frac{f E_c}{\delta - 3}\right) \quad (\text{B1})$$

where  $\alpha$  is the fine structure constant ( $\approx 1/137$ ),  $\Lambda$  is the Coulomb logarithm ( $\approx 20-30$  for fully ionized coronal plasma),  $z^2$  is the average coronal atomic number-squared ( $\approx 1.44$ ),  $m_e c^2 = 511$  keV,  $B$  is the Beta function,  $\delta$  is the electron flux power-law negative spectral index,  $E_c$  is the low-energy cutoff expressed in keV, and  $f$  is a slowly-varying function that depends mostly on  $\delta$ , and is equal to about 0.3 for  $\delta=4$ . For example, for  $\delta=4$  and  $E_c=10$  keV, one gets a bremsstrahlung emission efficiency of  $8.5 \times 10^{-6}$ . We have found good (within a 10–20%) correspondence with (exact) numerical computations.

### C. Magnetic field tilt estimation through simple geometry arguments

From the observation that radio sources seem to be displaced westward by  $\sim 2'$  on the average, we derive an average tilt angle of the magnetic field (or at least the direction of the main Type III emission) with the local radial to Sun center.



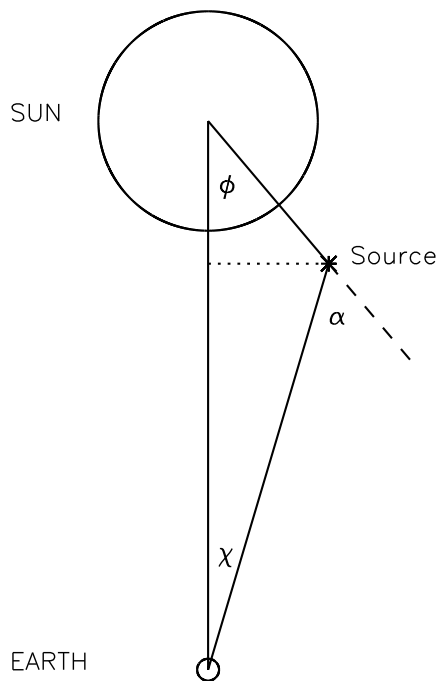


Fig. 17.— Type III emission geometry.

For simplicity, we consider in the following the geometry to be wholly within the ecliptic plane, and the Type III emission to have infinite directivity (zero beamwidth).

The “average” source is observed to be at a westward angle  $\chi$  from Sun center ( $\chi \approx 2'$ ), at an altitude  $R_S + h$ , where  $R_S$  is the solar radius. We call  $\phi$  the angle between the Sun-Earth line and the radial to the source, and  $\alpha$  the angle between the radial to the Sun and the direction in which the Type III is emitted (Figure 17). Then, the following must be true for the emission from the “average” source (which is near the solar surface) to be observed at Earth:

$$\alpha = \phi + \chi \quad (\text{C1})$$

A bit of trigonometry yields:

$$\sin(\phi) = \frac{D - (R_S + h) \cos(\phi)}{R_S + h} \tan(\chi) \quad (\text{C2})$$

where  $D$  is the Sun-Earth distance ( $\approx 215 R_S$ ). This is a transcendental equation which can be iteratively solved for  $\phi$ .  $\alpha$  is then simply derived from Eq C1. The following explicit formula, derived using simplified geometry,

$$\alpha \approx \chi + \arcsin\left(\frac{\chi \cdot D}{R_S + h}\right) \quad (\text{C3})$$

has accuracy better than 1% for  $h \leq 0.6 R_S$ .

Using  $\chi=2'$ , and for  $h$  between 0.1 and 0.5  $R_S$  (approximate altitude up to which decimetric emission can be found, cf. Figure 9), one obtains  $\alpha$  between 6.6 and 4.8 degrees. Say  $\alpha=6\pm 1$  degrees.

These results were derived from a very simple 2D model, assuming the Type III emission had infinite directivity. but they are in good agreement with the Monte-Carlo approach presented in Appendix D.

#### D. Magnetic field tilt estimation through a simple Monte-Carlo approach

In addition to the simple geometrical approach described in Appendix C, we ran a simple 3D simulation to estimate the effects of a tilt angle  $\alpha$  of the radio emission with respect to the local radial, the half-width  $\Delta\alpha$  of the cone of emission, and the source altitude  $h$ . A hundred thousand sources were uniformly distributed in longitude, but only within 15 and 30 degrees in latitude (which reflects reality). For each source, if Earth (and the observer) was within the cone of emission, the apparent position of the source on the Sun was recorded. If not, it was omitted. In Figure 18, we display the variations in averaged source East-West position, if one varies  $\alpha$ ,  $\Delta\alpha$ , or  $h$ .

Using canonical values of  $\alpha=6$  degrees,  $\Delta\alpha=30$  degrees, and  $h=0.5 R_S$ , one obtains a westward displacement of 137", i.e. very close to our reported observations. It can be said from Figure 18 that the result does not strongly depend on the exact value of  $h$ , i.e. a change of 0.1  $R_S$  leads to a change of the average displacement by  $\approx 10''$ . Reasonable ( $< 80$  degrees) values of  $\Delta\alpha$  lead to variations of up to  $\pm 25''$  at the most.

We conclude that the  $6\pm 1$  degrees tilt angle obtained in Appendix C is further validated by the simple 3-D model presented in this appendix.

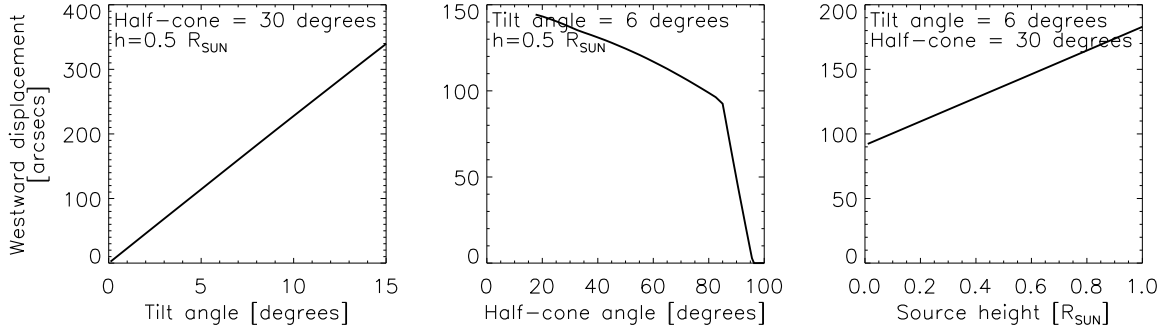


Fig. 18.— Westward displacement of the average source position, obtained through a Monte-Carlo simulation. See text for details.

### E. Rank-order correlations

Table 2 displays the Spearman Rank-order cross-correlation coefficients between burst parameters, for bursts observed at 164, 327, and 432 MHz. Spearman’s Rank-order cross-correlation acts on the *ranking* of the values instead of on their actual values, as a regular cross-correlation (e.g. Pearson’s) would. This has the huge advantage that even a non-linear (polynomial, exponential, power-law, etc.) relationship between parameter  $x$  and parameter  $y$  can achieve a cross-correlation coefficient near unity. The parameters are:

- $r$  is the angular distance to Sun center.
- $T_{B,true}$  is the peak brightness temperature (averaged over 10 s) of the deconvolved gaussian source (as described in Figure 10 and Section 3.1).
- $S_\nu$  is the burst flux (averaged over 10 s).
- $s_{true}$  is the FWHM size of the source, deconvolved as explained in Section 3.1.
- $\theta_{true}$  is the orientation of the semi-major axis of the source, from the map x-axis.
- $(a/b)_{true}$  is the ratio of the semi-major to semi-minor axis of the source, an easier quantity to visualize than the eccentricity.
- $s_{true,radial}/s_{true}$  is a measure of the source’s radial elongation, normalized to source rms size.
- $s_{true,azimuthal}/s_{true}$  is a measure of the source’s azimuthal elongation, normalized to source rms size.

Table 2: 164, 327, & 432 MHz rank-order cross-correlations between parameters.

	$r$	$T_{B,true}$	$S_\nu$	$s_{true}$	$\theta_{true}$	$(a/b)_{true}$	$\frac{s_{true,rad}}{s_{true}}$	$\frac{s_{true,azim}}{s_{true}}$
164 MHz								
$r$	1.00	-0.16	-0.07	0.28	0.00	0.18	-0.37	0.37
$T_{B,true}$	-0.16	1.00	0.90	-0.16	-0.00	-0.01	0.13	-0.02
$S_\nu$	-0.07	0.90	1.00	0.08	0.02	0.01	0.01	-0.01
$s_{true}$	0.28	-0.16	0.08	1.00	0.07	0.31	-0.13	0.24
$\theta_{true}$	0.00	-0.00	0.02	0.07	1.00	0.06	0.01	-0.02
$(a/b)_{true}$	0.18	-0.01	0.01	0.31	0.06	1.00	-0.34	0.45
$s_{true,radial}/s_{true}$	-0.37	0.13	0.01	-0.13	0.01	-0.34	1.00	-0.89
$s_{true,azimuthal}/s_{true}$	0.37	-0.02	-0.01	0.24	-0.02	0.45	-0.89	1.00
327 MHz								
$r$	1.00	-0.06	0.07	0.21	0.01	0.05	-0.34	0.34
$T_{B,true}$	-0.06	1.00	0.77	-0.21	-0.00	-0.06	0.11	0.00
$S_\nu$	0.07	0.77	1.00	0.29	0.04	0.01	-0.01	0.01
$s_{true}$	0.21	-0.21	0.29	1.00	0.07	0.25	-0.05	0.16
$\theta_{true}$	0.01	-0.00	0.04	0.07	1.00	-0.00	-0.01	-0.00
$(a/b)_{true}$	0.05	-0.06	0.01	0.25	-0.00	1.00	-0.22	0.34
$s_{true,radial}/s_{true}$	-0.34	0.11	-0.01	-0.05	-0.01	-0.22	1.00	-0.89
$s_{true,azimuthal}/s_{true}$	0.34	0.00	0.01	0.16	-0.00	0.34	-0.89	1.00
432 MHz								
$r$	1.00	-0.04	0.11	0.18	-0.02	0.05	-0.32	0.29
$T_{B,true}$	-0.04	1.00	0.71	-0.19	-0.03	-0.07	0.17	-0.00
$S_\nu$	0.11	0.71	1.00	0.35	0.04	-0.03	0.03	-0.00
$s_{true}$	0.18	-0.19	0.35	1.00	0.04	0.23	-0.03	0.20
$\theta_{true}$	-0.02	-0.03	0.04	0.04	1.00	-0.01	-0.01	-0.02
$(a/b)_{true}$	0.05	-0.07	-0.03	0.23	-0.01	1.00	-0.18	0.35
$s_{true,radial}/s_{true}$	-0.32	0.17	0.03	-0.03	-0.01	-0.18	1.00	-0.83
$s_{true,azimuthal}/s_{true}$	0.29	-0.00	-0.00	0.20	-0.02	0.35	-0.83	1.00

## REFERENCES

- Alvarez, H., & Haddock, F. T. 1973, *Sol. Phys.*, 29, 197
- Aschwanden, M. J. 2012, *A&A*, 539, A2
- Aschwanden, M. J., & Acton, L. W. 2001, *ApJ*, 550, 475
- Aschwanden, M. J., Tarbell, T. D., Nightingale, R. W., Schrijver, C. J., Title, A., Kankelborg, C. C., Martens, P., & Warren, H. P. 2000, *ApJ*, 535, 1047
- Bak, P., Tang, C., & Wiesenfeld, K. 1988, *Phys. Rev. A*, 38, 364
- Bastian, T. S. 1994, *ApJ*, 426, 774
- Benz, A. O., & Krucker, S. 2002, *ApJ*, 568, 413
- Bonnin, X., Hoang, S., & Maksimovic, M. 2008, *A&A*, 489, 419
- Bougeret, J.-L., Caroubalos, C., Mercier, C., & Pick, M. 1970, *A&A*, 6, 406
- Bougeret, J. L. 1981, *A&A*, 96, 259
- Brown, J. C. 1971, *Sol. Phys.*, 18, 489
- Cairns, I. H. 1987a, *Journal of Plasma Physics*, 38, 169
- Cairns, I. H. 1987b, *Journal of Plasma Physics*, 38, 179
- Cairns, I. H., Lobzin, V. V., Warmuth, A., Li, B., Robinson, P. A., & Mann, G. 2009, *ApJ*, 706, L265
- Caroubalos, C., & Steinberg, J. L. 1974, *A&A*, 32, 245
- Caroubalos, C., Poquerusse, M., & Steinberg, J. L. 1974, *A&A*, 32, 255
- Cash, W. 1979, *ApJ*, 228, 939
- Christe, S., Hannah, I. G., Krucker, S., McTierman, J., & Lin, R. P. 2008a, *ApJ*, 677, 1385
- Christe, S., Krucker, S., & Lin, R. P. 2008b, *ApJ*, 680, L149
- Coles, W. A., & Harmon, J. K. 1989, *ApJ*, 337, 1023
- Crawford, D. F., Jauncey, D. L., & Murdoch, H. S. 1970, *ApJ*, 162, 405
- Crosby, N. B., Aschwanden, M. J., & Dennis, B. R. 1993, *Sol. Phys.*, 143, 275
- David, C., Gabriel, A. H., Bely-Dubau, F., Fludra, A., Lemaire, P., & Wilhelm, K. 1998, *A&A*, 336, L90
- Dulk, G. A., Melrose, D. B., & Suzuki, S. 1979, *Proceedings of the Astronomical Society of Australia*, 3, 375
- Dulk, G. A., & Suzuki, S. 1980, *A&A*, 88, 203
- Dulk, G. A. 2000, in *Radio Astronomy at Long Wavelengths*, ed. R. G. Stone, K. W. Weiler, M. L. Goldstein, & J.-L. Bougeret, 115
- Dulk, G. A., Erickson, W. C., Manning, R., & Bougeret, J.-L. 2001, *A&A*, 365, 294
- Duncan, R. A. 1979, *Sol. Phys.*, 63, 389
- Eastwood, J. P., Wheatland, M. S., Hudson, H. S., Krucker, S., Bale, S. D., Maksimovic, M., Goetz, K., & Bougeret, J. 2010, *ApJ*, 708, L95
- Elgarøy, E. Ø. 1977, *Solar noise storms. (Solar noise storms., by Elgarøy, E. Ø.. International Series in Natural Philosophy (Oxford (UK): Pergamon Press), 13 + 363 p.)*
- Erickson, W. C. 1964, *ApJ*, 139, 1290
- Fainberg, J., & Stone, R. G. 1974, *Space Science Reviews*, 16, 145
- Fokker, A. D. 1963, *Bull. Astron. Inst. Netherlands*, 17, 214
- Fokker, Jr., A. D. 1960, PhD thesis, , Faculteit der Wis- en Natuurkunde, Leiden, (1960)
- Georgoulis, M. K., & Vlahos, L. 1996, *ApJ*, 469, L135+
- Hannah, I. G., Christe, S., Krucker, S., Hurford, G. J., Hudson, H. S., & Lin, R. P. 2008, *ApJ*, 677, 704

- Harrison, F. A., Christensen, F. E., Craig, W., Hailey, C., Baumgartner, W., Chen, C. M. H., Chonko, J., Cook, W. R., Koglin, J., Madsen, K.-K., Pivavoroff, M., Boggs, S., & Smith, D. 2005, *Experimental Astronomy*, 20, 131
- Higgins, P.A., Gallagher, P.T., Bloomfield, D.S., "A Study of Magnetic Features Over Solar Cycle 23", *A&A*, (in preparation).
- Hoang, S., Poquerusse, M., & Bougeret, J.-L. 1997, *Sol. Phys.*, 172, 307
- Hudson, H. S. 1991, *Sol. Phys.*, 133, 357
- Islaker, H., & Benz, A. O. 1994, *A&AS*, 104, 145
- Kerdraon, A., & Delouis, J.-M. 1997, in *Lecture Notes in Physics*, Berlin Springer Verlag, Vol. 483, *Coronal Physics from Radio and Space Observations*, ed. G. Trottet, 192–+
- Krucker, S., Oakley, P. H., & Lin, R. P. 2009, *ApJ*, 691, 806
- Le Squeren, A. M. 1963, *Annales d'Astrophysique*, 26, 97
- Lobzin, V. V., Cairns, I. H., Robinson, P. A., Steward, G., & Patterson, G. 2009, *Space Weather*, 7, 4002
- Lobzin, V., Cairns, I. H., & Robinson, P. A. 2011, *ApJ*, 736, L20
- Lu, E. T., & Hamilton, R. J. 1991, *ApJ*, 380, L89
- Mann, G., Jansen, F., MacDowall, R. J., Kaiser, M. L., & Stone, R. G. 1999, *A&A*, 348, 614
- Melrose, D. B. 1986, *Journal of Plasma Physics*, 36, 269
- Melrose, D. B. 1989, *Bulletin of the American Physical Society*, 34, 1293
- Mercier, C. 1986, *Journal of Atmospheric and Terrestrial Physics*, 48, 605
- Mercier, C., Subramanian, P., Kerdraon, A., Pick, M., Ananthakrishnan, S., & Janardhan, P. 2006, *A&A*, 447, 1189
- Mercier, C., & Trottet, G. 1997, *ApJ*, 474, L65+
- Morioka, A., Miyoshi, Y., Masuda, S., Tsuchiya, F., Misawa, H., Matsumoto, H., Hashimoto, K., & Oya, H. 2007, *ApJ*, 657, 567
- Newkirk, Jr., G. 1961, *ApJ*, 133, 983
- Nita, G. M., Gary, D. E., Lanzerotti, L. J., & Thomson, D. J. 2002, *ApJ*, 570, 423
- Parnell, C. E., & Jupp, P. E. 2000, *ApJ*, 529, 554
- Pick, M., & Ji, S. C. 1987, *Sol. Phys.*, 107, 159
- Pick, M., Maia, D., Kerdraon, A., Howard, R., Brueckner, G. E., Michels, D. J., Paswaters, S., Schwenn, R., Lamy, P., Llebaria, A., Simnett, G., Lanzerotti, L. J., & Aurass, H. 1998, *Sol. Phys.*, 181, 455
- Poquérusse, M., & McIntosh, P. S. 1995, *Sol. Phys.*, 159, 301
- Poquérusse, M., Hoang, S., Bougeret, J., & Moncuquet, M. 1996, in *American Institute of Physics Conference Series*, Vol. 382, *American Institute of Physics Conference Series*, ed. D. Winterhalter, J. T. Gosling, S. R. Habbal, W. S. Kurth, & M. Neugebauer, 62–65
- Ramesh, R., Kathiravan, C., Barve, I. V., Beeharry, G. K., & Rajasekara, G. N. 2010, *ApJ*, 719, L41
- Raoult, A., & Pick, M. 1980, *A&A*, 87, 63
- Robinson, P. A., Cairns, I. H., & Willes, A. J. 1994, *ApJ*, 422, 870
- Robinson, P. A., & Cairns, I. H. 1998, *Sol. Phys.*, 181, 363
- Saint-Hilaire, P., Krucker, S., & Lin, R. P. 2009, *ApJ*
- , 2010, *ApJ*, 721, 1933
- Shimizu, T. 1995, *PASJ*, 47, 251
- Steinberg, J. L., Hoang, S., & Dulk, G. A. 1985, *A&A*, 150, 205
- Stewart, R. T. 1974, *Sol. Phys.*, 39, 451
- Suzuki, K. 1961, *Tsuki*.
- Thejappa, G., MacDowall, R. J., & Bergamo, M. 2012, *ApJ*, 745, 187
- Vlahos, L., Georgoulis, M., Kluiving, R., & Paschos, P. 1995, *A&A*, 299, 897

Zheleznyakov, V. V., & Zaitsev, V. V. 1970, Soviet Ast., 14, 250

Zlobec, P., Messerotti, M., Dulk, G. A., & Kucera, T. 1992, Sol. Phys., 141, 165

We thank the referee for thoughtful comments on this manuscript. PSH was supported by NASA Heliospheric Guest Investigator grant NN07AH74G and NASA Contract No. NAS 5-98033. The NRH is funded by the French Ministry of Education, the French program on Solar Terrestrial Physics (PNST), the Centre National d'Etudes Spatiales (CNES), and the Région Centre. MV and AK acknowledge support from the CNES and the PNST. Special thanks to Anne Bouteille, Gordon Hurford, Hugh Hudson, Säm Krucker, and Jim McTiernan for discussions pertaining to this and other related work.

*Facilities:* Nançay Radioheliograph.